On the density profile of dark matter substructure in gravitational lens galaxies

Simona Vegetti[1] and Mark Vogelsberger[2]

[1] *Max Planck Institute for Astrophysics, Karl-Schwarzschild-Strasse 1, 85740 Garching, Germany*
[2] *Department of Physics, Kavli Institute for Astrophysics and Space Research, Massachusetts Institute of Technology, Cambridge, MA 02139, USA*

6 June 2014

ABSTRACT
We consider three extensions of the Navarro, Frenk and White (NFW) profile and investigate the intrinsic degeneracies among the density profile parameters on the gravitational lensing effect of satellite galaxies on highly magnified Einstein rings. In particular, we find that the gravitational imaging technique can be used to exclude specific regions of the considered parameter space, and therefore, models that predict a large number of satellites in those regions. By comparing the lensing degeneracy with the intrinsic density profile degeneracies, we show that theoretical predictions based on fits that are dominated by the density profile at larger radii may significantly over- or underestimate the number of satellites that are detectable with gravitational lensing. Finally, using the previously reported detection of a satellite in the gravitational lens system JVAS B1938+666 as an example, we derive for this detected satellite values of $r_{\max}$ and $v_{\max}$ that are, for each considered profile, consistent within 1σ with the parameters found for the luminous dwarf satellites of the Milky Way and with a mass density slope $\gamma < 1.6$. We also find that the mass of the satellite within the Einstein radius as measured using gravitational lensing is stable against assumptions on the substructure profile. In the future thanks to the increased angular resolution of very long baseline interferometry at radio wavelengths and of the E-ELT in the optical we will be able to set tighter constraints on the number of allowed substructure profiles.

Key words: galaxies: structure — gravitational lensing: strong

1 INTRODUCTION

Observations of the Milky Way satellite galaxies have long been used as test laboratories of the Cold Dark Matter (CDM) paradigm in the small non-linear regime. These have revealed a number of potential problems that include, *the missing satellite problem* (Klypin et al. 1999; Moore et al. 1999), *the core-cusp problem* (Moore 1994; Kuzio de Naray et al. 2008; de Blok 2010; Walker & Peñarrubia 2011; Amorisco & Evans 2012) and *the too big too fail problem* (Boylan-Kolchin et al. 2011, 2012). While some of these small-scale issues could potentially be solved by baryonic feedback processes and star formation (Governato et al. 2010, 2012; Brooks & Zolotov 2012), they may also be the signature of a different physics of the dark matter (e.g. Lovell et al. 2012; Vogelsberger et al. 2012).

As detecting satellite galaxies and measuring their properties can be observationally challenging, most of the observations have been limited to the Local Group, which may not necessarily be a fair representation of the Universe. It is therefore important to extend these observations to the satellite galaxies of other massive parent galaxies. Vegetti & Koopmans (2009a,b) have shown how highly magnified Einstein rings can be used to detect faint satellites in gravitational lens galaxies out to any lens redshift, and

how the measured properties of these satellites can be then used to constrain the mass function of mass substructure. This gravitational imaging technique detects mass substructure in lens galaxies via their gravitational effect on the surface brightness distribution of highly magnified Einstein rings and arcs. During this process, substructures are initially detected and their masses measured in a substructure-model independent way, that is, via pixelated potential corrections to a smooth potential model for the parent halo; subsequently, the data are remodelled within the context of a particular substructure model, and the most probable *a posteriori* values of the model parameters (e.g. the substructure mass, Einstein radius and position) given the data are determined. Generally, a singular isothermal sphere (SIS) or a truncated isothermal sphere are used for the substructure density profile. However, any other substructure model could in principle be used providing it produces the same gravitational lensing effect and fits the data equally well. Traditionally, substructures have been detected in lens galaxies via their effect on the magnification of multiply-imaged quasars (i.e. flux-ratio anomaly). However, due to the point-like nature of the lensed quasars, this type of data is not sensitive to individual substructures but to the general population. Flux ratio anomalies, therefore, cannot be used to constrain the substructure mass function

slope nor the density profile of each substructure, but can only be used to quantify the amount of substructures (Dalal & Kochanek 2002) or constrain the concentration of their mass density profile (Xu et al. 2012) in a statistical sense. In first approximation, gravitational lensing only provides a good measure of the mass within the Einstein radius of the lens. However, in combination with other observables (e.g. stellar dynamics and weak lensing) or if the lensed images have extended radial structure, a value for the *mean* density slope between the radial extend of the observations can also be derived (e.g. Koopmans et al. 2009; Barnabè et al. 2009; Newman et al. 2013; Grillo et al. 2013). At the scale of satellite galaxies Suyu & Halkola (2010) have shown that if a satellite galaxy is located close to a lensed arc with a radial extent larger or comparable to the size of the galaxy, the morphological structure of the arc contains important information that allow to constrain the mass distribution of the satellite. This is due to the fact that the satellites can affect the surface brightness distribution of the lensed images over their full radial extent. At the same time, however, it has been shown by Schneider & Sluse (2013) that due to the mass sheet degeneracy, combined with the lack of constraints over large regions of the lens plane, it is essentially not possible to measure the density profile of the deflector using only gravitational lensing.

In this Letter, we investigate the effect of different substructure density profiles on the surface brightness distribution of extended arcs. The aim is not to precisely measure the density profile of substructures but to quantify the degeneracies among different models and identify those regions of the profile parameter space that cannot reproduce the observed perturbation, hence set constraints on dark matter and/or galaxy formation models that predict a large number of subhaloes/satellites in those excluded regions. In practical terms, given that we know a SIS substructure profile to be a good description of the data (although not necessarily of the true underlying profile of the substructure), we will look for combinations of profile parameters that provide an equally good fit and for those that are instead excluded by the data. To this aim we consider different extensions of the NFW profile. Since we are studying the lensing effect of small substructures, which are more likely dark matter dominated, we believe this choice of profiles to be well justified. This method could provide an important test for models of dark matter. In Section 2, we define the lensing signature of satellites on gravitationally lensed images. In Section 3, we present the considered satellite mass models and their intrinsic degeneracies. Finally, in Sections 4 and 5 we discuss our results and summarize our main conclusions, respectively.

Throughout we assume a flat cosmology with $\Omega_{\rm m} = 0.25$, $\Omega_\Lambda = 0.75$ and $H_0 = 73 \, {\rm km \, s^{-1} \, Mpc^{-1}}$.

2   LENSING EFFECT

Given the surface brightness distribution $I(x)$ of the lensed images as a function of the position x on the lens plane, we define the effect of a given substructure as the difference in $I(x)$ between a lens that contains the substructure and the same smooth lens without the substructure, more precisely we consider

$$\mathcal{D} = \sum_x \left(\frac{B\,I_{\rm smooth}(x) - (B\,I_{\rm sub}(x) + n(x))}{2\,\sigma(x)} \right)^2. \qquad (1)$$

Here, B, is the blurring operator that encodes the effect of the telescope point-spread function and $n(x)$ is the observational Gaussian noise with standard deviation $\sigma(x)$. In general, the sensitivity of the gravitational imaging technique depends on the observational

Profile	σ_v [km s^{-1}]	r_s [kpc]	γ	r_c [kpc]	r_t/r_s
gNFW	15.6	0.1-5	0-2	-	-
gNFW$_2$	10-50	R_{200}/c_{200}	0-2	-	-
gtNFW	15.6	0.1-5	0-2	-	1-3
gtNFW$_2$	10-50	R_{200}/c_{200}	0-2	-	1-3
cNFW	15.6	0.1-5	1	0.1-5	-
cNFW$_2$	10-50	R_{200}/c_{200}	1	0.1-5	-

Table 1. The prior limits on the substructure parameters (velocity dispersion σ_v, scaling radius r_s, inner density slope γ, core radius r_c and truncation radius r_t) for all of the mass density profiles considered: a generalized NFW profile (gNFW), a generalized NFW profile with a given mass-concentration relation (gNFW$_2$), a generalized truncated NFW profile (gtNFW), a generalized truncated NFW profile with a given mass-concentration relation (gtNFW$_2$), a cored NFW profile (cNFW) and a cored NFW profile with a given mass-concentration relation (cNFW$_2$).

conditions as well as on the surface brightness distribution of the background source, and the substructure mass and position relative to the extended Einstein ring or arc.

Here, we test the specific case where all of these variables are matched to those found from an analysis of Keck adaptive optics imaging of the gravitational lens system JVAS B1938+666 (Lagattuta et al. 2012), where a substructure of mass $\sim 10^8$ M$_\odot$ was detected with the gravitational imaging technique at the 12σ confidence level (Vegetti et al. 2012). We leave a broader analysis of more general data properties, source models and substructure masses and positions to a forthcoming paper.

It should be noted that the lensing effect as defined in Equation (1) is essentially a χ^2, and is therefore proportional to the log-likelihood of the data ($B\,I_{\rm sub}(x) + n(x)$) given a smooth model ($B\,I_{\rm smooth}(x)$). It is known that this quantity can potentially lead to an over-estimate of the sensitivity to substructure of different masses and profiles. As it is shown by Vegetti et al. (2014), the effect of a substructure can be partly re-absorbed with a change in the source surface brightness structure and/or with a change in the lens macro model. This implies that the most rigorous way to quantify the sensitivity of a given substructure (model) is to compute the Bayes factor and marginalize over the lens and source parameters for a large number of mock data sets, each defined by a different combination of substructure mass models. Since this approach is computationally prohibitive and since in this Letter we are only interested in testing whether there is any observational signature to the mass density profile of the substructure under the simplest assumptions, we limit our study to consider the χ^2 above and refer to a future paper for a more rigorous quantification. Indeed, if the χ^2 is not sensitive to different mass models, this would be even more true for the Bayesian evidence. As an example, we re-model the mock data shown in the top right panel of Figure 1 with a SIS and a gNFW profile. By re-optimizing for the source, the main lens and the substructure parameters, we calculate the Bayesian evidence ($\mathcal{E}$) of both models and find that the gNFW model is preferred by a $\Delta \log \mathcal{E} \sim 120$, this corresponds roughly to a 15σ significance. The likelihood ratio, related to equation (1), is instead about 40 times larger (also in favour of the gNFW model). As expected, the degeneracy between the substructure, the lens macro model and the source structure can re-absorb the effect of a given substructure and reduce the difference among different profiles. In practice, we expect the shape of the degeneracy among several profiles to be essentially unaffected, while the size of the parameter region not compatible with the data to shrink or increase. Specifically, for a

given substructure mass and position, the size of the profile parameter space that is excluded by the data, at a given level of significance, is set by a combination of the data quality and the degeneracy between the substructure model and the macro model. Even though in this Letter, we have only used an approximation for the latter, our test shows our current analysis to be robust for combination of profile parameters with lensing effects that are significantly larger or smaller than the effect of the reference SIS profile. Moreover, we expect the loss of sensitivity due to re-absorption by the macro model to be compensated, in the future, by a gain in sensitivity thanks to a higher angular resolution of the data (e.g. VLBI and E-ELT) and the sizes of the allowed and dis-allowed regions to be close to what derived in this more simple approach.

3 SUBSTRUCTURE MASS MODEL

3.1 Parameterized mass models

For gravitational lens modelling, the most widely used parameterization of the total mass density profile is the SIS, which has a three-dimensional density distribution $\rho(r)$ given by

$$\rho(r) = \frac{\sigma_v^2}{2\pi G r^2} , \qquad (2)$$

where σ_v is the velocity dispersion, r is the radius and G is the gravitational constant. As well as the SIS, we also consider substructure models with three other different mass density profiles that are variations of the Navarro, Frenk & White (NFW; 1996a) model. They are the generalized NFW (gNFW), the truncated generalized NFW (gtNFW) and the cored NFW (cNFW) profiles.

A generalized formulation of the NFW density profile (gNFW) of arbitrary inner slope γ was introduced by Zhao (1996):

$$\rho(r) = \frac{\rho_s}{(r/r_s)^\gamma (1 + r/r_s)^{3-\gamma}} , \qquad (3)$$

where r_s is the scaling radius at which the slope of the density profile changes. The scaling radius is related to the concentration parameter c_{200}, introduced by Navarro et al. (1996b), and to the radius r_{200} that encloses a mass M_{200}, which has an over density of 200 above the critical density ρ_c, and is defined by

$$r_s = \frac{r_{200}}{c_{200}} = \left(\frac{3\, M_{200}}{800\, \pi\, \rho_c\, c_{200}^3} \right)^{1/3} . \qquad (4)$$

For $\gamma = 1$, this reduces to the classical NFW profile, while for $\gamma = 0$ we have an inner cored profile and for $\gamma = 2$ we have an isothermal profile.

Baltz et al. (2009) introduced a smoothly truncated NFW profile, that we extend here to the generalized case (gtNFW):

$$\rho(r) = \frac{\rho_s}{(r/r_s)^\gamma (1 + r/r_s)^{3-\gamma} (1 + (r/r_t)^2)^n} . \qquad (5)$$

Here, r_t is the truncation radius and n sets the sharpness of the truncation. In particular, we consider $n = 1$ and $r_t \geqslant r_s$.

We also consider a cored NFW profile (cNFW), as defined by Peñarrubia et al. (2012) to be

$$\rho(r) = \frac{\rho_s}{(r/r_s + r_c/r_s)(1 + r/r_s)^2} . \qquad (6)$$

In this case, r_c is the core radius, and for $r_c = 0$ this profile reduces to the classical NFW.

Generally, the main lensing properties, that is, the deflection angle $\alpha(x)$ and the surface mass density $\Sigma(x)$, of these profiles do not always have analytic expressions. These however, can be calculated numerically by solving for the integrals of the surface mass density,

$$\Sigma(x) = 2r_s \int_0^\infty \mathrm{d}z\, \rho\left(\sqrt{x^2 + z^2}\right), \qquad (7)$$

and the projected cylindrical mass,

$$M_{\mathrm{cyl}}(x) = 2\pi r_s^2 \int_0^x \mathrm{d}x'\, x'\, \Sigma\left(x'\right) . \qquad (8)$$

For a critical surface mass density,

$$\Sigma_c = \frac{c^2 D_s}{4\pi G D_{ds} D_d} , \qquad (9)$$

as a function of the angular diameter distances D_s to the source, D_d to the lens and D_{ds} between the lens and the source, the deflection angle is given by,

$$\alpha(x) = \frac{M_{\mathrm{cyl}}(x)}{\pi\, \Sigma_c\, x} . \qquad (10)$$

For all of the considered profiles, we set the normalization ρ_s by imposing a M_{200} mass equal to that of a SIS of given velocity dispersion σ_v,

$$M_{200} = \sigma_v^3 \left(\frac{3}{800\, \pi\, \rho_c} \right)^{1/2} \left(\frac{2}{G} \right)^{3/2} = \int_0^{r_{200}} \mathrm{d}r\, 4\pi r^2 \rho(r). \qquad (11)$$

In this way, we ensure that the substructures all have the same mass and that the comparison is meaningful. For the truncated profile of Equation (5), the normalization is obtained by integrating the non-truncated version of the profile. This can be done because we expect the M_{200} mass to be set at a time prior to the accretion of the satellite by the host galaxy. Once the normalization is fixed, all of the above models are left with two free parameters, which are sometimes degenerate with each other, as for example r_s and γ for the gNFW case.

Some of the considered values of the scaling radius can result in substructures that are more concentrated than the sub-haloes of the same mass that are seen in *N*-body CDM simulations. We therefore also consider cases where the velocity dispersion (and hence mass) changes, and the concentration is coupled to the mass by the mass-concentration relation defined by Duffy et al. (2008):

$$c_{200} = 5.71 \left(\frac{M_{200}}{2 \times 10^{12}\, h^{-1} M_\odot} \right)^{-0.084} (1 + z)^{-0.47} . \qquad (12)$$

The 12σ significance level detection of a mass substructure in the gravitational lens galaxy JVAS B1938+666 at $z = 0.881$ was obtained in a model independent way (Vegetti et al. 2012). This detection was shown to be consistent with a SIS that has $\sigma_v = 15.6$ km s^{-1}. In all of the considered cases above, we set the substructure velocity dispersion and redshift to these measured values, and investigate which combination of mass model parameters can result in a lensing effect (as defined by Equation 1) that is equal or comparable to what is produced by a SIS with these properties.

3.2 Intrinsic degeneracies

While Equation (1) can be used to quantify the degeneracy between the lensing effect and different substructure models, each of the above profiles suffer from intrinsic degeneracies in their main parameters. For example, the gNFW and the gtNFW can result in a high central density by having either a steep central slope γ or a
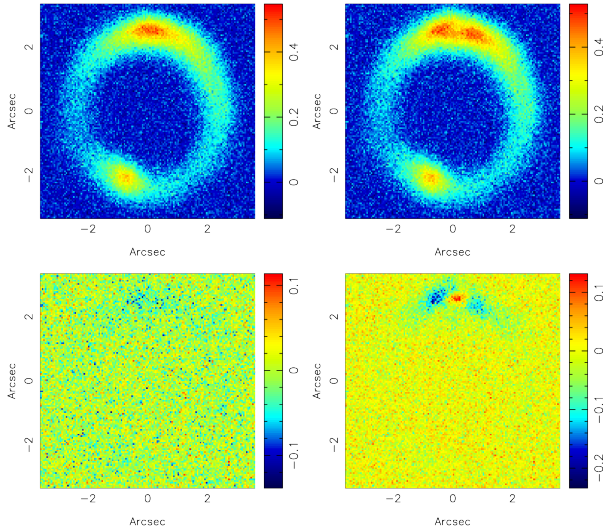
Figure 1. Top panels: mock data of the gravitational lens system JVAS B1938+666 with a SIS substructure (left) and a gNFW substructure (right) with the same mass, slope $\gamma = 0$ and scaling radius $r_s = 0.1$ kpc. Bottom panels: difference in the lensed images surface brightness distribution between a smooth version of the gravitational lens system JVAS B1938+666 and a substructures version with a SIS substructure (left) and a gNFW substructure (right) with the same mass, slope $\gamma = 0$ and scaling radius $r_s = 0.1$ kpc.

Profile	σ_v [km s^{-1}]	$r_{\max}$ [kpc]	$v_{\max}$ [km s^{-1}]	r_t/r_s
gNFW	-	5.0 ± 0.0	26.1 ± 0.0	-
gNFW$_2$	16.4 ± 2.6	-	-	-
gtNFW	-	0.9 ± 0.4	31.4 ± 5.1	1
gtNFW	-	1.9 ± 0.8	28.9 ± 4.8	2
gtNFW	-	2.6 ± 0.9	27.1 ± 5.1	3
gtNFW$_2$	23.9 ± 5.8	-	-	1
gtNFW$_2$	19.8 ± 4.3	-	-	2
gtNFW$_2$	18.8 ± 3.7	-	-	3
cNFW	-	5.0 ± 0.04	25.9 ± 0.1	-
cNFW$_2$	19.1 ± 1.5	-	-	-

Table 2. Derived kinematical properties for profiles with a lensing effect consistent with the observed SIS.

be expressed in terms of deflection profiles (i.e. $M(< r)/r$) since this is the quantity that gravitational lensing is constraining to first order.

large concentration parameter (i.e. small values of r_s), while the same effect can be achieved for a cNFW with either a small core or a large concentration. Following Wyithe, Turner & Spergel (2001), we quantify these intrinsic degeneracies by identifying those combinations of the $\rho(r)$ parameters that minimize the following relations, relative to a set of reference profiles ρ_0 of given slope γ (or core radius r_c) and different scaling radii r_s:

$$\chi^2_{rel} = \int_0^{r_{200}} r^2 \left(\frac{\rho(r) - \rho_0(r)}{\rho_0(r)} \right)^2 \mathrm{d}r \tag{13}$$

and

$$\chi^2 = \int_0^{r_{200}} r^2 \left(\rho(r) - \rho_0(r) \right)^2 \mathrm{d}r \,. \tag{14}$$

Specifically, for the gNFW and the gtNFW profiles, the reference profile ρ_0 is, respectively, a gNFW and a gtNFW with a slope fixed at $\gamma \equiv 1$ and with a scaling radius that is variable between the prior limits given in Table 1. For a cored NFW, ρ_0 is also a cored NFW with a fixed core of $r_c = 2$ kpc and with a scaling radius that is variable within the same prior range. As already pointed out by Wyithe et al. (2001), the minimization of the χ^2 is dominated by the central regions, so that a good fit is obtained for the central density at the cost of a poorer fit at larger radii. Conversely, the minimization of the χ^2_{rel} is dominated by the density at larger distances from the centre. For the truncated cases, the χ^2_{rel} is dominated by the regions around the truncation radius. In the attempt of providing predictions or performing comparisons between theoretical expectations and gravitational lensing observations based on analytic fits to the mass density distribution of numerically simulated subhaloes, it is, therefore, very important to choose the proper fitting metric. Suboptimal definitions of the minimizing function (i.e. χ^2_{rel} vs χ^2) can, in fact, lead to under-estimations or over-estimation of the subhalo gravitational lensing effect (see Section 4 and Fig. 2), and hence to biased results. In particular, the correct comparison metric should

4   DISCUSSION

The aim of this Letter is to investigate the gravitational lensing effect of different substructure profiles on the surface brightness distribution of extended gravitationally lensed images and determine which regions of the profile parameter space are in agreement or in disagreement with the observations. To investigate these degeneracies, we show in Fig. 2 the lensing effect of all of the considered profiles relative to the effect of a SIS profile, $\mathcal{D}/\mathcal{D}_{\mathrm{SIS}}$ (colour scale). The solid lines mark regions where the lensing signal of the profile under consideration is exactly the same as that expected for a SIS ($\mathcal{D}/\mathcal{D}_{\mathrm{SIS}} = 1$). This line represents mass density profiles that have the same (low) likelihood to be fit by a smooth model than the reference SIS substructure. The dashed lines mark those regions within which the lensing signal deviates less than $\pm$ 10 percent from the expected lensing signal of an SIS. What we see is that the lensing effect of the substructure as observed in JVAS B1938+666 is compatible with only a small combination of the different profile parameters, and that a large fraction of the parameter space can already be excluded. Tests with different noise levels, show that the signal-to-noise ratio of the data can broaden the ± 10 percent region around the $\mathcal{D}/\mathcal{D}_{\mathrm{SIS}} = 1$ curve, while leaving the shape of the latter essentially unaffected. This could break down in the case of significant covariance between the pixel noise, however we do not expect this to be the case for most ground based adaptive optics observations.

We find that gNFW models with low (high) concentrations and shallow (steep) central slopes produce lensing effects that are too small (large) to provide a good fit to the data and that all of the considered values for the core radius are possible as long as the cNFW profile is concentrated enough. In a future paper, we will investigate whether this is an indication that substructure lensing is insensitive to the size of the core radius or whether this is an issue related to the smoothness of the source surface brightness distribution considered here. For highly truncated profiles (e.g. gtNFW with $r_t = r_s$), the radial extent of the substructure is significantly suppressed and the lensing signal becomes essentially only sensitive to the mass within the truncation radius. This implies that the lensing effect is in this case insensitive to the concentration as long as the slope is steep enough to provide enough mass in the central regions of the substructure. As the truncation radius increases, a
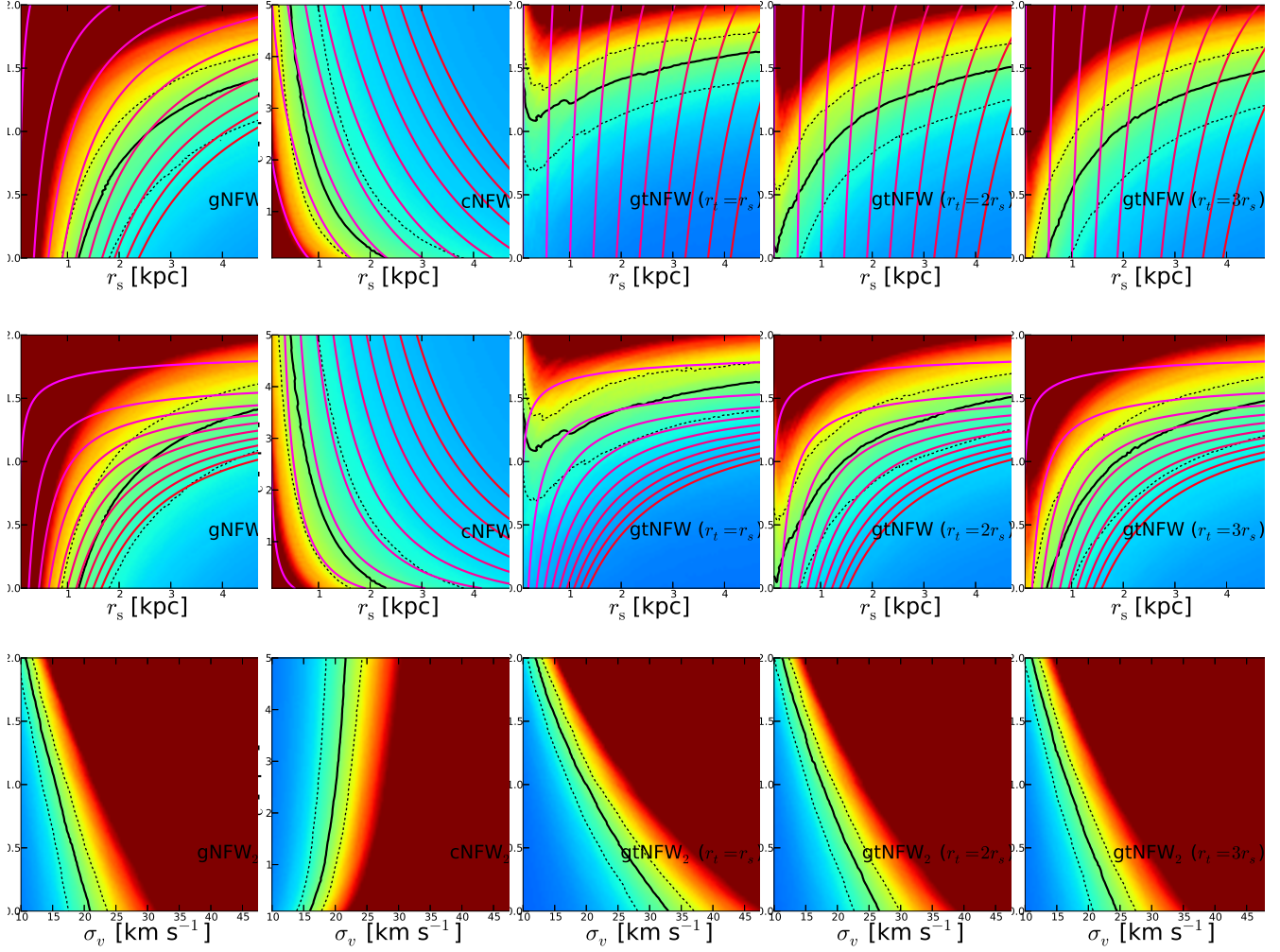
Figure 2. The degeneracy among the mass model parameters on the lensing effect $\mathcal{D}$ of a substructure with different profiles (as indicated). The solid line indicates the region of the parameter space where the considered substructure profile has the same lensing effect as a SIS ($\mathcal{D} = \mathcal{D}_{\mathrm{SIS}}$), while the dashed lines indicate the deviation from the solid line by ± 10 percent. The solid red lines are iso-χ^2_{rel} (top panels) and iso-χ^2 (middle panels) lines and indicate the intrinsic degeneracy among the different mass profile parameters. The colour scale is the quantity $\mathcal{D}$ normalized to $\mathcal{D}_{\mathrm{SIS}}$.

larger range of slope is allowed, while the lensing signal becomes slowly more sensitive to the scaling radius.

Independently of the profile, we derive an upper limit on the mass density slope of $\gamma < 1.6$.

We now focus on the mass and kinematical properties of these profiles. Even though the lensing signal still shows an intrinsic degeneracy in the main model parameters, only profiles with a tight range of r_{max} and v_{max} combinations are consistent with the reference SIS. In particular, by considering all of the combinations of profile parameters that lead to $\mathcal{D}/\mathcal{D}_{\mathrm{SIS}} = 1$, we derive a mean values of $r_{\mathrm{max}} = 3.1$ kpc and $v_{\mathrm{max}} = 28.5$ km s^{-1} (see Table 2 for more details). We find, therefore, that the substructure properties of JVAS B1938+666 are consistent only with profiles that have kinematical properties within 1σ from those of the bright dwarf spheroidal satellite galaxies of the Milky Way (Boylan-Kolchin et al. 2011). This is not an obvious result, since the host lens is a massive early-type galaxy at z = 0.881, and has therefore a mass which is much larger than the Milky-Way. The bottom panels of Fig. 2 show the lensing degeneracy among various profiles of different masses, but with the same concentration.

From the $\mathcal{D}/\mathcal{D}_{\mathrm{SIS}} = 1$ regions on these plots, we find that that the substructure velocity dispersion is constrained to a relatively tight range between 13.8 km s^{-1} and 29.8 km s^{-1} (see Table 2 for more details). From all the profiles with $\mathcal{D}/\mathcal{D}_{\mathrm{SIS}} = 1$, we then derive an average mass within 300 pc of $M_{300} = 8.3 \times 10^7~M_\odot$ with an rms of $1.4 \times 10^8~M_\odot$. This is consistent with the mass of the substructure found in JVAS B1938+666, as measured by Vegetti et al. (2012) under the assumption of a pseudo-Jaffe profile, $M_{300} = 1.13 \pm 0.06 \times 10^7~M_\odot$. Within each of the different profiles, we find smaller scatters and larger errors (relative to a SIS) for the substructure mass, but these are always consistent with the results of Vegetti et al. (2012). Finally, we derive an average projected mass within the Einstein of $M_{\mathrm{E}} = 3.2 \times 10^6 M_\odot$. This is also comparable with the mass within the Einstein radius of the reference SIS $M_{\mathrm{SIS}} = 4 \times 10^6 M_\odot$. This indicates that substructure lensing provides a reliable measure of the main substructure properties independently on the assumed profile and that the gravitational imaging technique provides a precise measure of the lensing mass. We can therefore conclude that the substructure mass function derived with the gravitational imaging technique is not biased

by our assumption on the form of the substructure density profile at least relative to the detections.

Different dark-matter models make different predictions for the density profile of galaxy haloes and sub-haloes. In order to compare these theoretical expectations with the gravitational lensing observations, it is important to understand how the corresponding degeneracies behave relative to each other. The top and middle panels of Fig. 2 show the lensing degeneracy along with the intrinsic profile degeneracy that is obtained by minimizing the χ^2_{rel} and the χ^2, respectively. We find that those predictions that are based on fits dominated by the density profile at large radii, could significantly over- or under-estimate the lensing effect and, therefore, the predicted number of substructures that are observable with gravitational lensing. This is particularly true for truncated profiles, where the two forms of degeneracies become almost orthogonal to each other.

5 CONCLUSIONS

In this Letter, we have investigated the gravitational lensing effect of different substructure models on highly magnified Einstein rings. Our main results can be summarized as follows i) the gravitational imaging technique can be used to exclude large regions of the considered parameter space and therefore models that predict a large number of satellites in those regions; ii) only profiles with the right level of central concentration provide a good fit to the data; iii) given the signal-to-noise ratio and angular resolution of the data, and the source surface brightness distribution considered here, the gravitational lensing effect of mass substructure is essentially insensitive to the size of cores; iv) even at the substructure level gravitational lensing provides a precise measure of the lensing mass; v) independent of the assumed mass profile, substructure observations in the gravitational lens galaxy B1938+666, are consistent with values of $r_{\max}$ and $v_{\max}$ that are within 1σ of the values derived for the luminous dwarf satellites of the Milky Way and a mass density slope $\gamma < 1.6$; vi) a theoretical prediction based on fits that are dominated by the density profile at larger radii may significantly over or under-estimate the number of substructure detectable with lensing.

In light of these results we can conclude that substructure lensing provides an important tool to explore the density profiles of galaxy satellites beyond the local Universe. We stress once more, that the results presented in this Letter are based on specific assumptions on the substructure mass and location on the arc and on the substructure sensitivity. We have also made specific assumptions on the observational quality of the lensed images to those made with ground based adaptive optics on a 10-m class telescope (see Vegetti et al 2012 and Lagattuta et al 2012). We refer to a future paper for a wider analysis that takes into account more general physical and observational scenarios. Thanks to the increased angular resolution, we expect to be able to put tighter constraints on the number of allowed substructure profiles in the near term using very long baseline interferometry at radio wavelengths of extended arcs, and in the more distant future with the E-ELT.

REFERENCES

Amorisco N. C., Evans N. W., 2012, MNRAS, 419, 184
Baltz E. A., Marshall P., Oguri M., 2009, JCAP, 1, 15
Barnabè M., Czoske O., Koopmans L. V. E., Treu T., Bolton A. S., Gavazzi R., 2009, MNRAS, 399, 21
Boylan-Kolchin M., Bullock J. S., Kaplinghat M., 2011, MNRAS, 415, L40
Boylan-Kolchin M., Bullock J. S., Kaplinghat M., 2012, MNRAS, 422, 1203
Brooks A. M., Zolotov A., 2012, arXiv:1207.2468
Dalal N., Kochanek C. S., 2002, ApJ, 572, 25
de Blok W. J. G., 2010, Advances in Astronomy, 2010
Duffy A. R., Schaye J., Kay S. T., Dalla Vecchia C., 2008, MNRAS, 390, L64
Governato F., Brook C., Mayer L., Brooks A., Rhee G., Wadsley J., Jonsson P., Willman B., et al., 2010, Nature, 463, 203
Governato F., et al., 2012, MNRAS, 422, 1231
Grillo C., Christensen L., Gallazzi A., Rasmussen J., 2013, MNRAS, 433, 2604
Klypin A., Kravtsov A. V., Valenzuela O., Prada F., 1999, ApJ, 522, 82
Koopmans L. V. E., Bolton A., Treu T., Czoske O., Auger M. W., Barnabè M., Vegetti S., Gavazzi R., Moustakas L. A., Burles S., 2009, ApJL, 703, L51
Kuzio de Naray R., McGaugh S. S., de Blok W. J. G., 2008, ApJ, 676, 920
Lagattuta D. J., Vegetti S., Fassnacht C. D., Auger M. W., Koopmans L. V. E., McKean J. P., 2012, MNRAS, 424, 2800
Lovell M. R., Eke V., Frenk C. S., Gao L., Jenkins A., Theuns T., Wang J., White S. D. M., et al., 2012, MNRAS, 420, 2318
Moore B., 1994, Nature, 370, 629
Moore B., Ghigna S., Governato F., Lake G., Quinn T., Stadel J., Tozzi P., 1999, ApJL, 524, L19
Navarro J. F., Frenk C. S., White S. D. M., 1996a, ApJ, 462, 563
Navarro J. F., Frenk C. S., White S. D. M., 1996b, ApJ, 462, 563
Newman A. B., Treu T., Ellis R. S., Sand D. J., Nipoti C., Richard J., Jullo E., 2013, ApJ, 765, 24
Peñarrubia J., Pontzen A., Walker M. G., Koposov S. E., 2012, ApJL, 759, L42
Schneider P., Sluse D., 2013, A&A, 559, A37
Suyu S. H., Halkola A., 2010, A&A, 524, A94
Vegetti S., Koopmans L. V. E., 2009a, MNRAS, 392, 945
Vegetti S., Koopmans L. V. E., 2009b, MNRAS, 400, 1583
Vegetti S., Koopmans L. V. E., Auger M. W., Treu T., Bolton A. S., 2014, MNRAS, submitted
Vegetti S., Lagattuta D. J., McKean J. P., Auger M. W., Fassnacht C. D., Koopmans L. V. E., 2012, Nature, 481, 341
Vogelsberger M., Zavala J., Loeb A., 2012, MNRAS, 423, 3740
Walker M. G., Peñarrubia J., 2011, ApJ, 742, 20
Wyithe J. S. B., Turner E. L., Spergel D. N., 2001, ApJ, 555, 504
Xu D. D., Mao S., Cooper A. P., Gao L., Frenk C. S., Angulo R. E., Helly J., 2012, MNRAS, 421, 2553
Zhao H., 1996, MNRAS, 278, 488